Nanoscale Advances

ROYAL SOCIETY OF CHEMISTRY

PAPER

View Article Online
View Journal | View Issue

Cite this: *Nanoscale Adv.*, 2025, **7**, 4876

Interfacial S-scheme charge transfer in $MgIn_2S_4$/ZnO heterojunction for enhanced photodegradation of tetracycline and efficient water splitting†

Tunde L. Yusuf, *[a] Olalekan C. Olatunde,[bf] Daniel Masekela,[c] Oluwaseyi D. Saliu,[de] Kwena Desmond Modibane[c] and Damian C. Onwudiwe[bf]

Environmental pollution and high energy costs are among today's most pressing global challenges. Photocatalysis offers a cost-effective and environmentally sustainable strategy to address these issues by enabling efficient pollutant degradation and hydrogen production. This work constructed a nanoflower $MgIn_2S_4$ and nanorod ZnO heterojunction to enhance photocatalytic performance through an interfacial S-scheme charge transfer mechanism. Unlike most reported ZnO-based heterojunctions in the literature, this approach introduces $MgIn_2S_4$, a ternary sulfide with a narrow band gap and a high conduction band potential, to form a heterostructure material with a strong redox potential and efficient charge separation. The $MgIn_2S_4$/ZnO heterojunction exhibited superior photocatalytic activity, achieving a remarkable 94% tetracycline (TCE) degradation efficiency, 1.4 and 3.9 times higher than that of pristine $MgIn_2S_4$ and ZnO, respectively. Furthermore, the heterojunction demonstrated an improved hydrogen evolution rate of 8.29 mmol h^{-1} g^{-1}, significantly surpassing ZnO (6.96 mmol h^{-1} g^{-1}) and $MgIn_2S_4$ (6.24 mmol h^{-1} g^{-1}). The enhanced performance is attributed to the efficient interfacial charge transfer, as confirmed by X-ray photoelectron spectroscopy (XPS) analysis and electrochemical characterization, demonstrating charge migration from $MgIn_2S_4$ to ZnO. Mechanistic investigations further revealed that the S-scheme charge transfer mechanism effectively promoted charge separation and facilitated the generation of reactive radical species, ultimately leading to improved photocatalytic activity. This study highlights the potential of the rationally designed $MgIn_2S_4$/ZnO S-scheme heterojunction as a highly efficient and sustainable photocatalyst for organic pollutant degradation and hydrogen production under visible light irradiation, providing a promising solution to environmental and energy challenges.

Received 11th June 2025
Accepted 23rd June 2025

DOI: 10.1039/d5na00573f

rsc.li/nanoscale-advances

Introduction

The increasing demand for clean energy and the rising concern over environmental pollution have spurred the search for sustainable and efficient methods to address both issues. Among the various pollutants, organic contaminants are particularly harmful due to their persistence in the environment, contributing to water and soil pollution.[1,2] The quest for clean energy, mainly hydrogen, has also gained significant traction as a viable alternative to fossil fuels.[3] Photocatalysis offers a promising dual-function solution by utilizing sunlight to degrade organic pollutants while simultaneously generating hydrogen, a clean energy carrier.[4–6] However, the efficiency of photocatalysts remains a significant challenge, prompting the exploration of innovative materials and strategies.[7–9]

Recently, the development of heterojunction photocatalysts has emerged as a successful strategy for enhancing the separation of photogenerated electron–hole pairs, a critical factor in improving photocatalytic performance.[10–13] Among these, S-

[a]Department of Chemistry, Faculty of Natural and Agricultural Sciences, University of Pretoria, Private Bag X20, Hatfield 0028, Pretoria, South Africa. E-mail: yusuf.tl@up.ac.za

[b]Material Science Innovation and Modelling (MaSIM) Research Focus Area, Faculty of Natural and Agricultural Sciences, Mafikeng Campus, North-West University, Private Bag X2046, Mmabatho 2735, South Africa

[c]Department of Chemistry, University of Limpopo, Sovenga, Polokwane, 0727, South Africa

[d]Department of Chemical Engineering, University of Illinois, 929 W Taylor St, Chicago, Illinois 60607, USA

[e]Department of Industrial Chemistry, University of Ilorin, Permanent Site, Tanke, Ilorin 234031, Nigeria

[f]Department of Chemistry, School of Physical and Chemical Sciences, Faculty of Natural and Agricultural Sciences, North-West University, Mafikeng Campus, Private Bag X2046, Mmabatho 2735, South Africa

† Electronic supplementary information (ESI) available. See DOI: https://doi.org/10.1039/d5na00573f

scheme heterojunctions have gained attention due to their unique band alignment, which promotes spatial charge separation while retaining strong redox abilities.[14–17] This allows for more efficient degradation of pollutants and enhanced hydrogen evolution. The combination of $MgIn_2S_4$, a ternary chalcogenide with excellent photocatalytic properties, and ZnO, a well-established photocatalyst, represents a promising S-scheme heterojunction for environmental remediation and hydrogen production.

$MgIn_2S_4$ is an emerging ternary metal sulfide. It has garnered interest for its suitable band gap, high light absorption efficiency, and chemical stability, making it an ideal candidate for visible-light-driven photocatalysis [18,19] It has a narrow band gap of 1–9–2.2 eV and a very high conduction band of 1.2–0.7 eV.[20] This high conduction band makes it a suitable reduction photocatalyst.[21] However, its performance is often hindered by the rapid recombination of electron–hole pairs. On the other hand, ZnO possesses a wide bandgap and superior charge transport properties, but is limited in its ability to utilize visible light.[22,23] Advances in ZnO-based heterojunctions have revealed improved photocatalytic performance by materials such as Ag_2O–ZnO,[24] and MnS/ZnO.[25] However, the potential synergy between ZnO and ternary metal sulphides such as $MgIn_2S_4$ has not been significantly explored in photocatalytic processes. Coupling $MgIn_2S_4$ with ZnO in an S-scheme heterojunction allows for the preservation of holes with strong oxidation potential in the valence band of ZnO and the conduction band electrons of $MgIn_2S_4$ with superior reduction ability. This configuration results in improved visible light absorption, preservation of high redox potential, and enhanced spatial separation of charge carriers.

In this study, we report the rational design and fabrication of an S-scheme $MgIn_2S_4$/ZnO heterojunction for the dual application of organic pollutant degradation and hydrogen production. The heterojunction was carefully designed to optimize the interfacial charge transfer between $MgIn_2S_4$ and ZnO, facilitating efficient photocatalytic reactions under visible light irradiation. We employed a series of characterization techniques, including X-ray diffraction (XRD), scanning electron microscopy (SEM), and UV-visible diffuse reflectance spectroscopy (UV-vis DRS), to elucidate the structural and optical properties of the heterojunction.

The photocatalytic performance of the $MgIn_2S_4$/ZnO heterojunction was evaluated by degrading organic pollutants and producing hydrogen through water splitting under visible light. The results demonstrated a significant enhancement in pollutant degradation and hydrogen evolution compared to the individual components. These findings highlight the potential of the rationally designed S-scheme heterojunction as an effective solution for addressing environmental pollution and the global energy crisis.

Experiment

Synthesis of photocatalyst

Synthesis of ZnO. A stirring solution of sodium hydroxide (1.0 g, 0.5 moles) was prepared, to which zinc acetate dihydrate $Zn(CH_3COO)_2 \cdot 2H_2O$ (4 g, 1.0 mole) was added, resulting in the formation of a white colloidal solution. The mixture was stirred for 1 hour and then transferred to a Teflon-lined autoclave. It was subsequently heated in a furnace at 180 °C for 24 hours. The resulting precipitate was collected by centrifugation and washed three times each with water and ethanol. Finally, the precipitate was dried overnight in an oven at 70 °C.

Synthesis of $MgIn_2S_4$/ZnO heterojunction. 1 mmol of the synthesized ZnO was dispersed in 60 mL of deionized water through ultrasonication for 15 minutes. To this solution, 0.2 mmol of $Mg(NO_3)_2 \cdot 6H_2O$, 0.4 mmol of $InCl_3$, and 0.9 mmol of L-cysteine were added, followed by continuous stirring for 1 hour. The resulting mixture was then transferred to a Teflon-lined autoclave and heated in a furnace at 180 °C for 24 hours. The precipitate formed was collected by centrifugation and washed three times each with deionized water and ethanol. Finally, the precipitate was dried overnight in an oven at 70 °C.

Characterization

Photocatalytic test. The photocatalytic degradation of tetracycline (10 mg L^{-1}, 50 mL) was carried out using 100 W xenon solar lamp-placed 10 cm above the solution's surface-as the light source. Initially, 30 mg of the catalyst was dispersed in the pollutant-containing solution and stirred in the dark for 30 minutes to establish adsorption–desorption equilibrium. Following this, the light was turned on, and 3 mL samples were collected at predetermined intervals. These samples were then centrifuged at 7000 rpm for 10 minutes to separate the catalyst efficiently. The resulting supernatant was analyzed using a UV-visible spectrophotometer. Each photooxidation experiment was performed in triplicate.

The efficiency of the degradation process was estimated using the percentage degradation (eqn (1)):

$$\%\ \text{Degradation} = \left(1 - \frac{C_t}{C_0}\right) \times 100\% \quad (1)$$

where, C_0 amd C_t (mg L^{-1}) are the initial and final concentration of the pollutant after a particular reaction time(t). The catalyst's recyclability was assessed by washing it three times with deionized water, followed by drying at 80 °C for five hours before reuse in subsequent experiments. The total organic carbon (TOC) removal of was estimated on a Shimadzu TOC-V analyzer.

During the photocatalytic water-splitting process, 100 mg of the catalyst was dispersed in a sealed reaction cell containing 50 mL of distilled water (Scheme S1†). The reaction was initiated using a 150 W Osram lamp. A 50 mL gas syringe was employed to measure the volume of the generated hydrogen and oxygen gases. The ideal gas law, which assumes both gases behave ideally, was applied to calculate the amount of H_2 gas produced.

Radical scavenging experiment. Scavenger experiments were performed to determine the key reactive species involved, utilizing 0.2 mmol L^{-1} of sodium EDTA, isopropanol (IPA), and benzoquinone. These quenchers specifically targeted holes (h^+), hydroxyl radicals ($^{\bullet}OH$), and superoxide radicals ($O_2^{\bullet-}$), respectively.

Results and discussion

The crystal structure and composition of $MgIn_2S_4$, ZnO, and $MgIn_2S_4$/ZnO heterojunctions were studied using X-ray diffraction. Fig. 1a shows the XRD pattern for $MgIn_2S_4$, ZnO, and $MgIn_2S_4$/ZnO heterojunction. The pattern of $MgIn_2S_4$ reveals prominent diffraction peaks at 2θ values 27.4, 33.2, 44.0, and 48.3, which correspond respectively to the (311), (400), (511) and (440) planes of cubic $MgIn_2S_4$ phase (JCPDS No.: 31-0792).[18,26] The sharp and distinct peaks of the XRD pattern showed that a well-crystallized $MgIn_2S_4$ structure was obtained. The XRD pattern of ZnO is consistent with the hexagonal wurtzite phase of ZnO with lattice parameters $a = b = 0.324$ nm and $c = 0.521$ nm (JCPDS No: 36.1451).[27,28] The XRD pattern of $MgIn_2S_4$/ZnO showed the co-existence of $MgIn_2S_4$ and ZnO in the heterojunction. Furthermore, a significant positive shift of the $MgIn_2S_4$ peaks towards higher angles compared to the pristine $MgIn_2S_4$. This strong shift could be attributed to strong interfacial interaction, which increased lattice strain and, consequently, shifted towards higher angles.[29]

The morphology of the materials was studied through their SEM and TEM images. The SEM image of $MgIn_2S_4$ shows spherical particles with rough surface texture. It's likely composed of densely packed nanosheets or a porous network, while ZnO displayed agglomerated particles with less defined shapes. The particles appear clustered with some visible small round grains. The SEM image of $MgIn_2S_4$/ZnO shows the sheet-like morphology of $MgIn_2S_4$ alongside some darker elongated structures corresponding to ZnO nanorods. This suggests a close interfacial contact between the layered $MgIn_2S_4$ and ZnO. The TEM images (Fig. reveal a sheet-like structure with well-defined edges in $MgIn_2S_4$, indicating a 2D morphology, whereas ZnO exhibits a rod-like structure with a high aspect ratio. The 2D structure of $MgIn_2S_4$ and ZnO's characteristics structure show morphological properties optimized for photocatalytic activity. Furthermore, the relatively uniform dispersion of ZnO within the $MgIn_2S_4$ matrix provides more active sites for catalytic activity, improving the heterojunction's TCE degradation.

The textural properties of the prepared catalysts were explored using N_2 adsorption–desorption isotherms. As shown

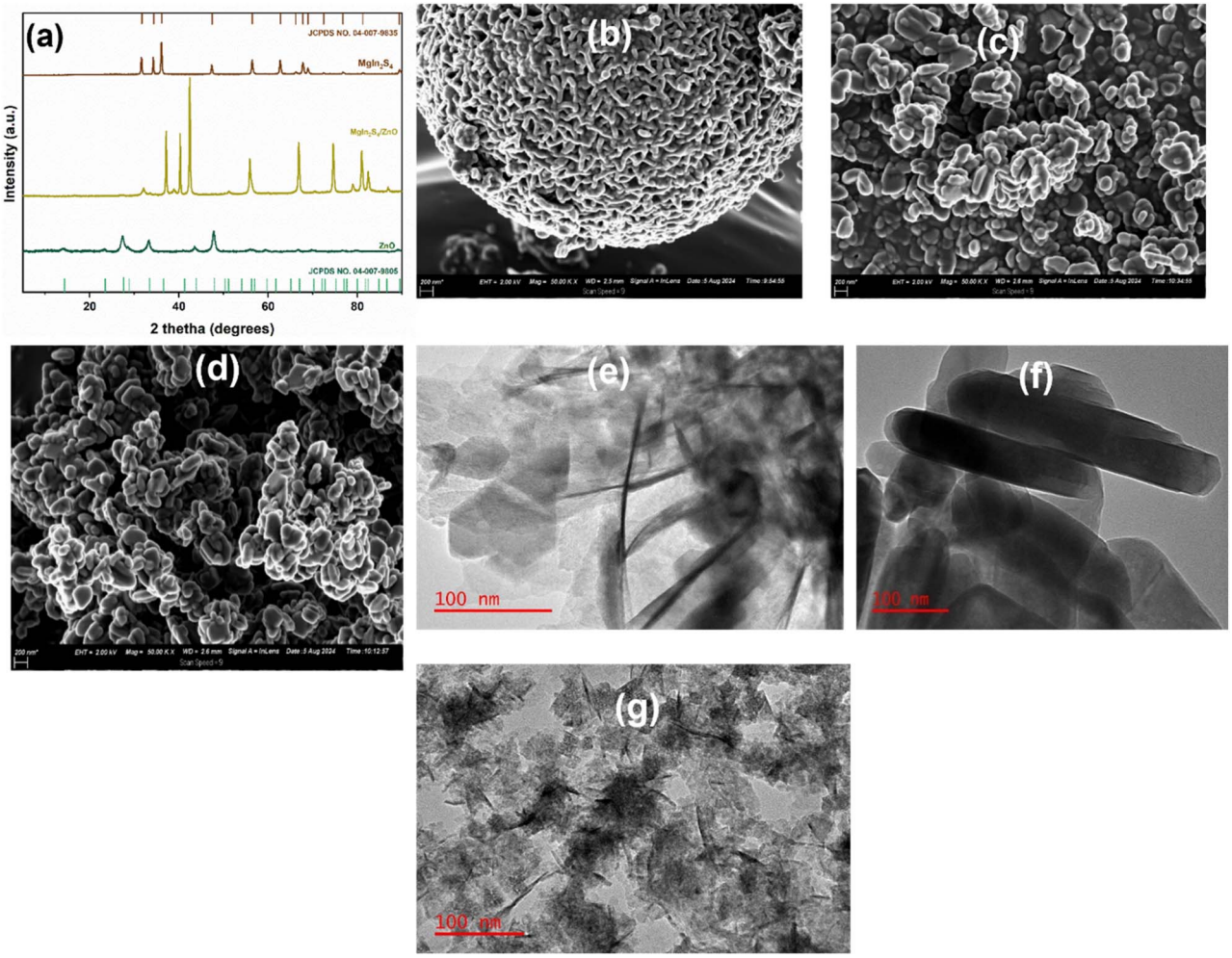

Fig. 1 (a) XRD spectra of $MgIn_2S_4$, ZnO, and $MgIn_2S_4$/ZnO, SEM images for (b) $MgIn_2S_4$, (c) ZnO, and (d) $MgIn_2S_4$/ZnO, and TEM Images for (e) $MgIn_2S_4$, (f) ZnO, and (g) $MgIn_2S_4$/ZnO.

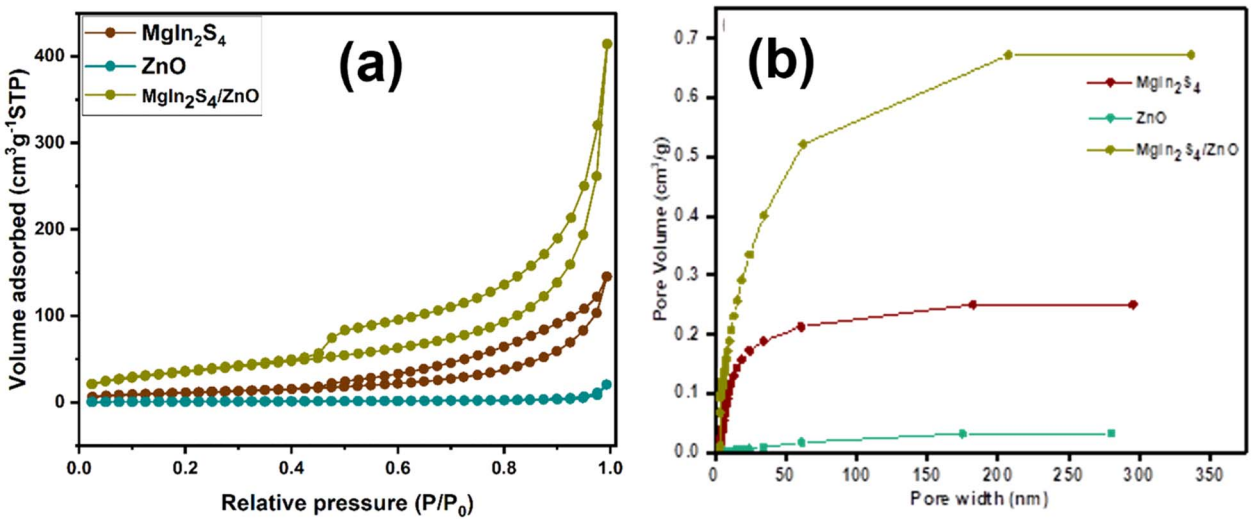

Fig. 2 (a) BET plot for $MgIn_2S_4$, ZnO, and $MgIn_2S_4$/ZnO heterojunctions (b) the pore size distribution plot for the catalysts.

in Fig. 2, adsorption–desorption isotherms of the $MgIn_2S_4$, ZnO, and $MgIn_2S_4$/ZnO presented type IV curves. The shape of the loop of $MgIn_2S_4$ and $MgIn_2S_4$/ZnO isotherms suggests a Type H3 hysteresis, which is indicative of mesoporosity and the presence of irregular pores.[30] Furthermore, $MgIn_2S_4$/ZnO showed a more pronounced hysteresis than $MgIn_2S_4$ due to its enhanced microporosity, which resulted in enhanced pore formation. In ZnO, no visible hysteresis was observed, suggesting the presence of micropores. Table 1 presents a summary of the textural parameters of the catalysts. The BET surface area of $MgIn_2S_4$/ZnO was higher than $MgIn_2S_4$ and ZnO, signifying a beneficial synergism in the construction of the heterojunction. High surface area implies the presence of more active sites for photocatalytic activity, which could be pivotal for the photocatalytic degradation of organic pollutants and the hydrogen evolution reaction. Fig. 2b shows the pore size distribution plot for the catalysts. The mesoporosity observed for $MgIn_2S_4$ and $MgIn_2S_4$/ZnO and the microporosity observed for ZnO aligns with the observation from the BET plot. $MgIn_2S_4$/ZnO showed the highest pore volume and a broad pore size distribution compared to the pristine materials, confirming the heterojunction's synergistic effect on the material's textural properties.

The surface chemistry and elemental composition of pristine $MgIn_2S_4$, ZnO, and $MgIn_2S_4$/ZnO heterojunction were elucidated by X-ray photoelectron spectrometry (XPS) spectra (Fig. 3). The survey scan of the three compounds (Fig. 3a) shows the presence of Mg, In, S in $MgIn_2S_4$; Zn, and O in ZnO and confirms the coexistence of $MgIn_2S_4$ and ZnO in the heterojunction with the presence of Mg, In, S, Zn and O in the spectra of $MgIn_2S_4$/ZnO. Additionally, the core-level spectra of Zn 2p, Zn 3p, O 1s, Mg 1s, In 3d, and S 2p were investigated. The high-resolution spectra of Mg 1s (Fig. 3b) show a single peak at 1340.5 eV in $MgIn_2S_4$, while a shift to higher binding energy (1344.8 eV) was observed in $MgIn_2S_4$/ZnO, which could be assigned to Mg^{2+} oxidation state of $MgIn_2S_4$.[18,31] The peaks observed in the In 3d spectra at 444.3 eV and 451.9 eV could be attributed to $3d_{3/2}$ and In $3d_{5/2}$ of $MgIn_2S_4$, respectively. In the spectra of $MgIn_2S_4$/ZnO, these peaks were observed at higher binding energies of 452.6 eV and 441.6 eV (Fig. 3c) [32] The S $2p^{1/2}$ and S $2p^{3/2}$ peaks of S^{2-} appeared at 161.1 eV and 164.1 eV, respectively. In the spectra of $MgIn_2S_4$/ZnO, these peaks were detected at a higher binding energy[33] (Fig. 3d). Fig. 3e shows the binding energy of the Zn $2p_{3/2}$ of ZnO was shifted from 1022.2 eV in ZnO to 1020.7 eV in $MgIn_2S_4$/ZnO. The O 1s core-level spectrum of ZnO shows the presence of two different forms of oxygen. The peak observed at ~529.4 eV could be assigned to O^{2-} ions of lattice oxygen, while the peak at 531.0 eV is related to chemisorbed oxygen on the ZnO surface [34] The O 1s spectra were also observed to be shifted towards lower binding energy in the spectra of $MgIn_2S_4$/ZnO (Fig. 3f). The shift in the binding energy observed in the spectra of the $MgIn_2S_4$/ZnO may be attributed to the change in the electron density resulting from the interfacial interaction between $MgIn_2S_4$ and ZnO. The shift in the binding energy of Mg, In, and S to a higher binding energy, while those of Zn and O in ZnO shifted to lower energy, suggests the transfer of electrons from $MgIn_2S_4$ to ZnO in the $MgIn_2S_4$/ZnO heterojunction.

The UV-vis spectroscopy was performed in the 200–800 nm range to explore the optical absorption behaviors of $MgIn_2S_4$, ZnO, and $MgIn_2S_4$/ZnO heterojunction. As shown in Fig. 4a, $MgIn_2S_4$ exhibited a sharp absorption which extends into the visible light range with an absorption edge of ~600 nm. For ZnO, a sharp absorption in the UV range with an absorption edge around ~370 nm was observed. The absorption edge

Table 1 Textural characteristics of $MgIn_2S_4$, ZnO and $MgIn_2S_4$/ZnO

Material	Surface area ($m^2\ g^{-1}$)	Pore volume ($cm^3\ g^{-1}$)	Pore diameter (nm)
$MgIn_2S_4$	45.26	0.22	10.07
ZnO	2.84	0.032	3.32
$MgIn_2S_4$/ZnO	101.81	0.62	3.14

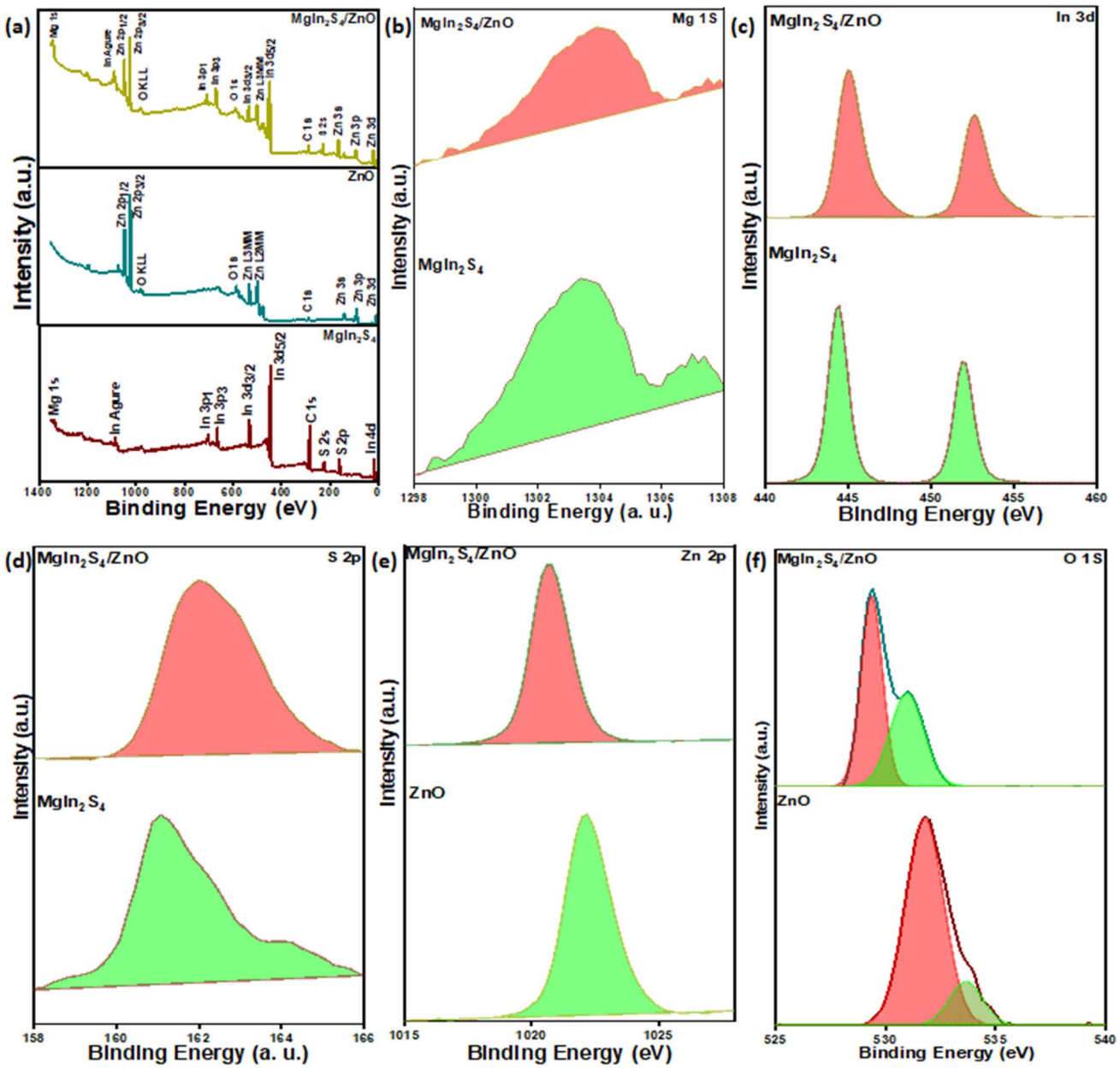

Fig. 3 (a) Survey scan of $MgIn_2S_4$, ZnO, and $MgIn_2S_4$/ZnO (b) high resolution scan of Cu 2p (c) In 3d (d) S 2p (e) Ce 3d (f) O 1s.

corresponds to ZnO characteristic wide band gap. The absorption of $MgIn_2S_4$/ZnO was intermediate between that of $MgIn_2S_4$ and ZnO, with a band edge around ~450 nm, suggesting a band structure modification. According to the Tauc plot, the band gap energies (E_g) of $MgIn_2S_4$ and ZnO are 2.16 and 3.24 eV, respectively, as shown in Fig. 4(b and c), which are in agreement with values reported in the literature.[35,36]

The Mott–Schottky (MS) plot was employed in determining the valence band (E_{vb}) and conduction band (E_{cb}) positions of $MgIn_2S_4$ (Fig. 4d) and ZnO (Fig. 4e). The flat band potentials (V_{fb}) were calculated using the Mott–Schottky equation (eqn (2)):

$$\frac{1}{C^2} = \frac{2}{A^2 e \mathcal{E} \mathcal{E}_o N_A}\left(E - V_{fb} - \frac{k_B T}{e}\right), \quad (2)$$

where parameters C, A, e, ε, ε_o, N_A, k_B, and T represent the interfacial capacitance, electrode surface, electronic charge, dielectric constant, free space permittivity, carrier concentration, applied voltage, Boltzmann constant, and absolute temperature, respectively. The positive slope of the E–C^2 plot showed that the materials are n-type semiconductors.[37] From the MS plot, the flat band potential (E_{fb}) of both materials was estimated to be −1.11 and −0.48 eV *vs.* NHE for $MgIn_2S_4$ and ZnO, respectively. This translates to E_{fb} values of −0.91 and −0.28 eV *vs.* NHE for $MgIn_2S_4$ and ZnO, respectively, using the Nernst equation – $E_{NHE} = E_{Ag/AgCl} + 0.197$. Furthermore, since the E_{cb} of n-type semiconductors is about 0.1–0.2 eV above the E_{fb}, the E_{cb} for both materials is therefore estimated to be −1.11 and −0.48 eV, for $MgIn_2S_4$ and ZnO, respectively.[38]

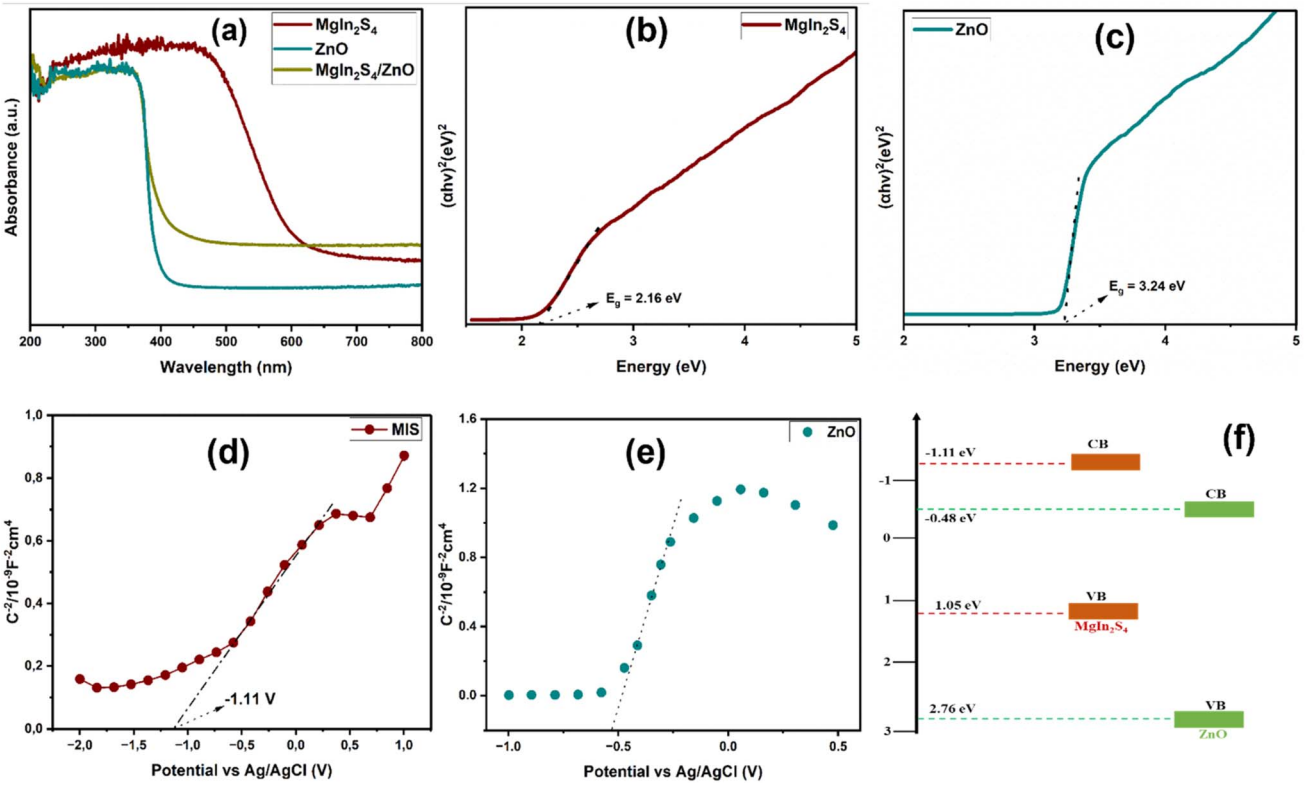

Fig. 4 (a) UV-vis spectra of ZnO, $MgIn_2S_4$, and $MgIn_2S_4$/ZnO heterojunctions. Tauc plot for (b) ZnO, (c) $MgIn_2S_4$, and Mott–Schottsky plot for (d) $MgIn_2S_4$ and (e) ZnO and (f) band alignment in $MgIn_2S_4$/ZnO heterojunction.

Furthermore, the expression $E_{cb} = E_{vb} - E_g$, The E_{vb} of $MgIn_2S_4$ and ZnO are estimated to be 1.05 eV and 2.76 eV, respectively. Based on the estimated E_{cb} and E_{vb}, the band alignment in the $MgIn_2S_4$/ZnO heterojunction was observed to be the sandwich band alignment structure, as depicted in Fig. 4f.

In the development of photocatalytic materials, charge carrier properties such as charge lifetime, diffusion length, and recombination rate are crucial factors. Modifying these properties is essential for enhancing photocatalytic performance. Electrochemical impedance spectroscopy (EIS) and current density measurements were utilized to investigate the charge carrier characteristics of the materials. Fig. 5a presents the EIS spectra of $MgIn_2S_4$, ZnO, and $MgIn_2S_4$/ZnO. The semicircle in the EIS spectra provides valuable insights into charge carrier separation, transport, and the resistance of photo-generated charge carriers. The semi-circle of EIS spectra gives important information on the charge carrier separation, transport, and resistance of photo-generated charge carriers. Since the radius of the EIS arc is inversely correlated to the charge-transfer resistance at the electrode–electrolyte interface, the $MgIn_2S_4$/ZnO heterojunction possesses lower charge-transfer resistance compared to the pristine $MgIn_2S_4$ and ZnO. This showed

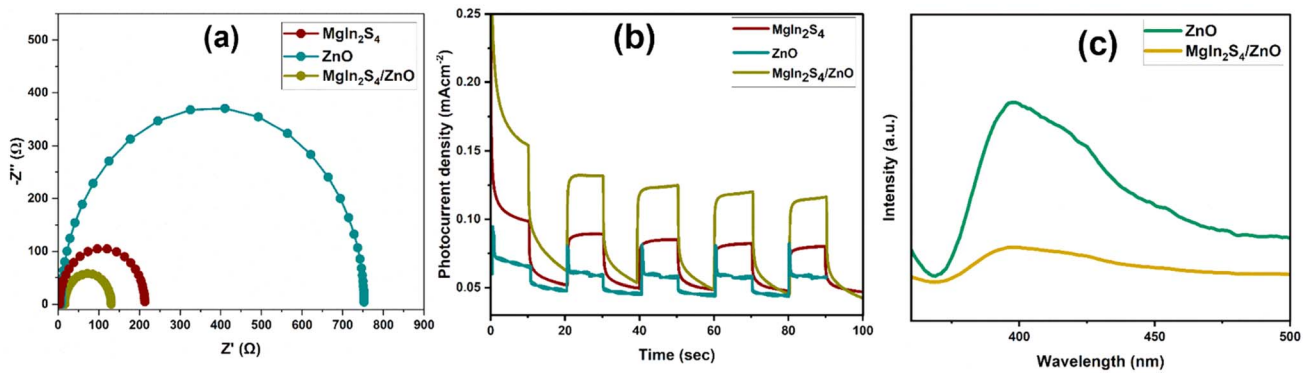

Fig. 5 (a) EIS spectra of $MgIn_2S_4$, ZnO, and $MgIn_2S_4$/ZnO heterojunction (b) Photocurrent density of $MgIn_2S_4$, ZnO, and $MgIn_2S_4$/ZnO heterojunction (c) Photoluminescence spectra of $MgIn_2S_4$, ZnO, and $MgIn_2S_4$/ZnO (excited at 325 nm).

$MgIn_2S_4$/ZnO heterojunction's improved charge carrier separation. Materials showing enhanced charge carrier properties often show enhanced photocurrent charge density. The enhanced photocurrent charge density displayed $MgIn_2S_4$/ZnO (Fig. 5b) supports the observation from the EIS spectra, thus confirming the improved charge carrier properties of the heterojunction. The charge carrier density of the $MgIn_2S_4$/ZnO heterojunction was almost twice the values for both pristine materials, showing the heterojunction's enhanced charge carrier characteristics. These enhanced charge carrier characteristics are highly important for the enhancement of photocatalytic activity. The photoluminescence (PL) spectra of the samples also confirmed the improved charge properties of the heterojunction material. Compared to ZnO, the heterojunction showed a significantly reduced PL intensity, which implies an improved charge carrier separation (Fig. 5c).

Photocatalytic activity

Degradation of tetracycline. Tetracycline is a widely used antibiotic that accesses the environment through several routes, including agricultural practices, wastewater treatment plants, and pharmaceutical manufacturing. Its presence in the environment can have significant environmental impacts, such as toxicity to aquatic organisms, bioaccumulation, and antibiotic resistance. Consequently, tetracycline (TCE) was explored as a model pollutant to evaluate the photocatalytic performance of the catalysts. The photocatalytic degradation efficiency of TCE by $MgIn_2S_4$/ZnO was assessed and compared with those of ZnO and $MgIn_2S_4$, as shown in Fig. 6. From Fig. 6a, the stability of TCE under direct irradiation was observed, with no significant degradation observed. However, in the presence of $MgIn_2S_4$/ZnO, the efficiency of TCE removal reached 94%, significantly higher than those of ZnO (68%) and $MgIn_2S_4$ (34%). The corresponding kinetics plots are shown in Fig. 6b, which reveals the linear relationship between $-\ln(C/C_o)$ and irradiation time. This implies the degradation of TCE by $MgIn_2S_4$/ZnO followed a pseudo-first-order kinetics.[39] The highest photodegradation rate constant (k) was recorded for $MgIn_2S_4$/ZnO (0.174 min^{-1}), which was approximately 4 and 30 times higher than those of ZnO (0.0405 min^{-1}) and $MgIn_2S_4$ (0.00575 min^{-1}). This result reveals that the $MgIn_2S_4$/ZnO heterojunction benefited from the improved charge carrier properties resulting from the interfacial interaction, leading to the formation of the heterojunction. Furthermore, the efficiency of mineralization of TCE measured through the TOC reached ~65% (Fig. 6c), which shows the potential of the $MgIn_2S_4$/ZnO heterojunction in mineralizing TCE to H_2O and CO_2. Table 2 shows a comparison of the degradation efficiency of other ZnO-based heterojunctions with the $MgIn_2S_4$/ZnO heterojunction. The efficiency attained by $MgIn_2S_4$/ZnO is comparable to other reported materials.

Process variables often play a significant role in the efficiency of the photocatalytic process. Therefore, the influence of process variables – catalyst dosage and pH – on the degradation of TCE by $MgIn_2S_4$/ZnO was evaluated. Fig. 6d shows the influence of catalyst dosage on the efficiency of TCE degradation. The degradation efficiency improved as the amount of the catalyst increased, which could be attributed to improved charge carrier generation arising from increased active sites. Solution pH is a very important factor that influences the surface properties of the photocatalyst and the behavior of the

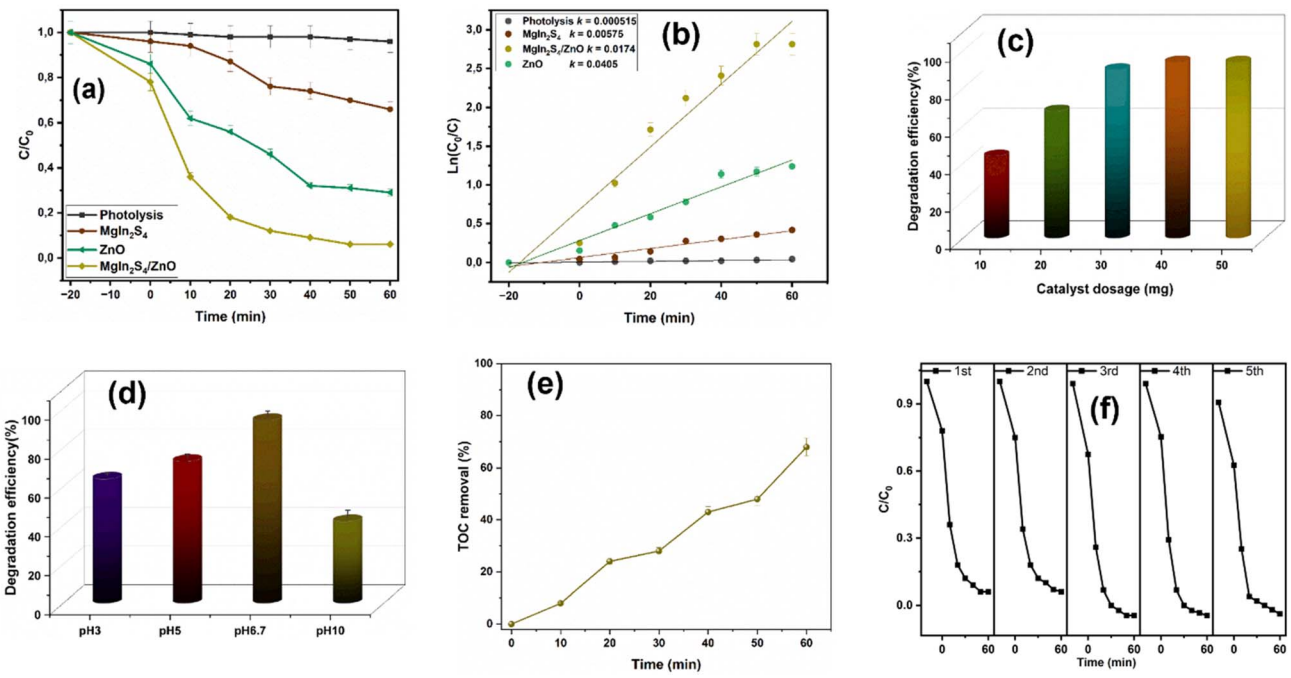

Fig. 6 (a) Photocatalytic degradation profile of TCE by $MgIn_2S_4$, ZnO, and $MgIn_2S_4$/ZnO, (b) pseudo-first order kinetics plot for TCE degradation, (c) the effect of catalyst dosage on the degradation of TCE (d) the effect of pH on the degradation of TCE (e) TOC removal by $MgIn_2S_4$/ZnO in synthetic and real water samples (f) reusability of the $MgIn_2S_4$/ZnO heterojunction over five consecutive experimental cycles for the photocatalytic degradation of TCE.

Table 2 Comparison of TCE degradation of $MgIn_2S_4$/ZnO with other ZnO-based heterojunctions reported in the literature

Catalyst	Catalyst dosage	TCE parameters	Degradation efficiency (%)	Rate (min^{-1})	Ref.
$LaCoO_3$/ZnO	10 mg L^{-1}	40 mg L^{-1}; 50 mL; 120 min	90.0	1.79×10^{-2}	22
ZnO/γ-Fe_2O_3	10 mg L^{-1}	30 mg L^{-1}; 20 mL; 150 min	88.5	1.32×10^{-3}	40
ZnO/Cus	10 mg	30 mg L^{-1}; 25 mL; 60 min	85.3	3.20×10^{-2}	41
ZnO/K-$Cn_{0.5}$	50 mg	50 mg L^{-1}; 100 mL; 60 min	90.0	3.49×10^{-2}	42
$MgIn_2S_4$/ZnO	30 mg	10 mg L^{-1}; 50 mL; 60 min	94.0	4.05×10^{-2}	This study

pollutant. Fig. 6e reveals the impact of pH on TCE degradation by $MgIn_2S_4$/ZnO. The degradation was highest at near-neutral pH 6.7. The degradation was significantly reduced at alkaline pH, which suggests a reduction in the interaction between the pollutant and the catalyst surface at this pH. Consequently, the stability of the catalyst was evaluated by conducting the experiment over five consecutive cycles for the photocatalytic degradation of TCE under visible light irradiation Fig. 6f. The catalyst demonstrated excellent stability, maintaining nearly the same degradation efficiency throughout all five cycles.

Photocatalytic H_2 evolution activity

The hydrogen evolution performance of the $MgIn_2S_4$ZnO heterojunction was systematically evaluated under visible light irradiation, with the variation in photocatalytic hydrogen evolution (PHE) over time shown in Fig. 7a. The production of H_2 increased linearly with irradiation time, demonstrating that hydrogen evolution was continuous and stable throughout the reaction. The heterojunction photocatalyst exhibited significantly higher hydrogen evolution activity than its individual components, particularly within the first 2 hours, highlighting the superior efficiency of the composite material.

To quantify the improvement, the hydrogen evolution rate (HER) of the heterojunction was compared with its pristine counterparts (Fig. 7b). The $MgIn_2S_4$/ZnO heterojunction achieved an HER of 8.29 mmol h^{-1} g^{-1}, which was notably higher than that of ZnO (6.96 mmol h^{-1} g^{-1}) and $MgIn_2S_4$ (6.24 mmol h^{-1} g^{-1}). The substantial increase in HER confirms the successful formation of an efficient heterojunction, which enhances charge separation and suppresses recombination, leading to improved photocatalytic activity. The improved hydrogen evolution rate of the $MgIn_2S_4$/ZnO heterojunction is primarily attributed to the synergistic interaction between the two components. Individually, both ZnO and $MgIn_2S_4$ have inherent limitations. ZnO, despite its high electron mobility, suffers from rapid electron–hole recombination, reducing its overall photocatalytic efficiency. On the other hand, $MgIn_2S_4$ has a relatively narrow bandgap, making it more susceptible to photocorrosion and charge recombination. By forming an S-scheme heterojunction, these drawbacks are mitigated, leading to a 19.1% improvement in HER over ZnO and a 32.8% increase compared to $MgIn_2S_4$.

Photocatalytic mechanism

Radical scavenging experiments were carried out to investigate the mechanism of photogenerated charge carrier transport. The investigation was carried out in the presence of Na-EDTA, benzoquinone (BQ), and isopropyl alcohol (IPA) as hole (h^+), superoxide ($O_2^{\bullet-}$), and hydroxyl ($^{\bullet}OH$) radical scavengers, respectively. From Fig. 8a, it could be observed that the $O_2^{\bullet-}$ had the most impact on TCE degradation by $MgIn_2S_4$/ZnO. The photogenerated h^+ and $^{\bullet}OH$ also exhibited an appreciable impact on the degradation efficiency. This affirms the enhanced charge carrier dynamics in the $MgIn_2S_4$/ZnO due to the formation of a heterojunction.

Based on the scavenging result and the band alignment scheme presented earlier, the charge transfer mechanism of TCE degradation by $MgIn_2S_4$/ZnO is shown in Fig. 8b. Generally,

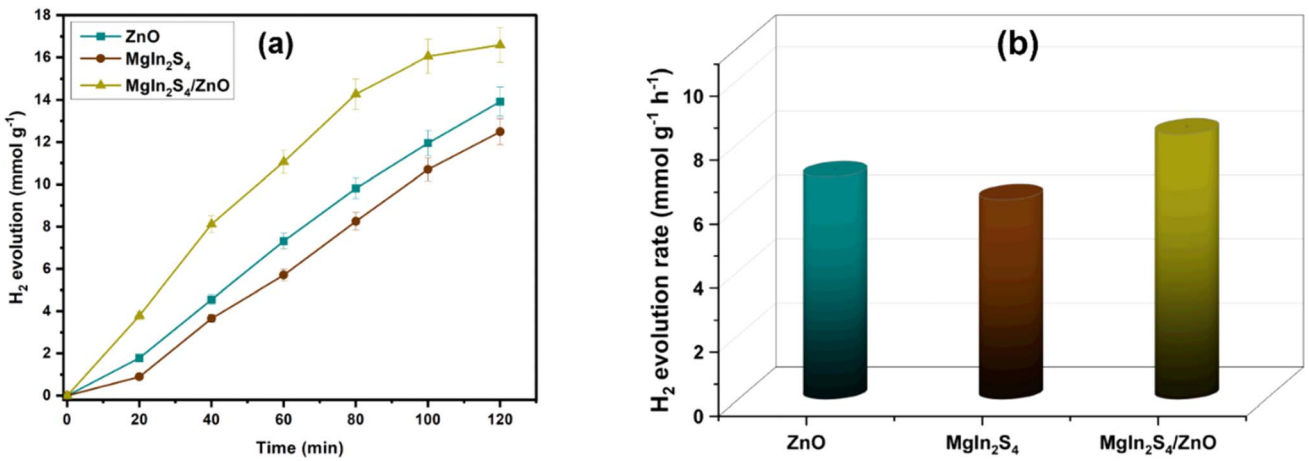

Fig. 7 (a) H_2 evolution with time and (b) the H_2 evolution rate of $MgIn_2S_4$, ZnO, and $MgIn_2S_4$/ZnO.

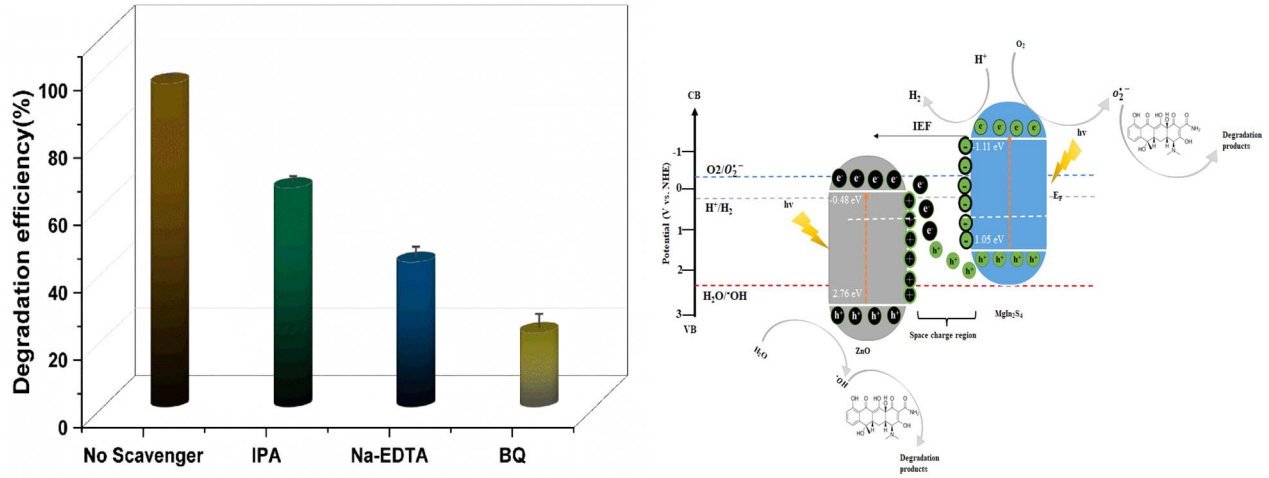

Fig. 8 Radical scavenging experiment (left), and proposed S-scheme charge transfer mechanism for $MgIn_2S_4$/ZnO heterojunction (right).

materials with lower Fermi energy serve as the oxidation photocatalyst, while material with higher Fermi energy serves as the reduction catalyst. The work function of ZnO and $MgIn_2S_4$ have been reported to be 4.7 eV and 4.4 eV, respectively. Therefore, when both materials come into contact, there is a spontaneous transfer of electrons from $MgIn_2S_4$ to ZnO until the equilibration of the Fermi energies, which consequently leads to bending of the bands in both materials.[43,44] Additionally, the charge transfer creates an internal electric field (IEF) at the interface, which is oriented from $MgIn_2S_4$ to ZnO. The transfer of electrons from $MgIn_2S_4$ to ZnO is supported by the XPS analysis, which confirms the direction of electron transfer. Under light irradiation, photogenerated h^+ and e^- are generated in the CB and VB of both catalysts. Influenced by the synergistic activity of the IEF, coulomb interaction, and band edge bending, e^- from the CB of ZnO recombines with h^+ from the VB of $MgIn_2S_4$, leading to the preservation of the highly active e^- on the CB of $MgIn_2S_4$ and highly oxidative h^+ in the VB of ZnO. This proves that the $MgIn_2S_4$/ZnO is an S-scheme heterojunction.[45]

The photogenerated holes in the VB of ZnO are lower than the $H_2O/^{\bullet}OH$ potential (2.76 eV). They are therefore capable of generating $^{\bullet}OH$, which can oxidize the pollutants due to their strong oxidative power. Also, the holes have sufficiently low potential to oxidize adsorbed pollutants directly.[46] Additionally, the CB of $MgIn_2S_4$ has a higher potential (−1.11 eV) than $O_2/O_2^{\bullet-}$ (−0.33 eV), which makes the photogenerated photoelectrons capable of reducing surface O_2 to generate $O_2^{\bullet-}$, which, owing to their strong oxidative potential, are capable of oxidizing the pollutant.[47] The photogenerated electrons on the CB of $MgIn_2S_4$ are also capable of generating hydrogen through the splitting of water.[48] Therefore, the S-scheme mechanism of the $MgIn_2S_4$/ZnO heterojunction not only enhanced the charge carrier dynamics of the photocatalyst but also optimized the redox potential of the material for effective pollutant degradation and H_2 generation.

Therefore, TCE oxidation takes place at the CB of $MgIn_2S_4$, while the h^+ in the VB of ZnO is captured by H_2O to form $O_2^{\bullet-}$ and direct interaction between TCE and h^+ could also take place at the VB of ZnO as suggested by the radical scavenging experiment.

Conclusion

This work reports the synthesis of a novel S-scheme $MgIn_2S_4$/ZnO heterojunction photocatalyst using a facile hydrothermal method. The establishment of the S-scheme charge transfer mechanism between $MgIn_2S_4$ and ZnO resulted in an enhanced light absorption capacity and improved charge carrier separation. The $MgIn_2S_4$/ZnO photocatalyst demonstrated enhanced photocatalytic activity under visible light for TCE degradation (94% after 60 min) and hydrogen production (8.29 mmol h^{-1} g^{-1}). Furthermore, the material demonstrated excellent stability, retaining its activity after 5 cycles, indicating its suitability for practical applications. The radical scavenging experiment revealed that the activity of the photocatalyst was induced by $^{\bullet}OH$, $O_2^{\bullet-}$, and h^+ radicals.

Data availability

The data supporting this study's findings are available from the corresponding author upon reasonable request. The datasets generated during and/or analyzed during the current study are not publicly available but are available from the corresponding author on reasonable request. Additionally, ESI data† and materials can be found in the ESI files† associated with this publication.

Conflicts of interest

There is no conflict to declare.

Acknowledgements

The authors gratefully acknowledge the financial support provided by the Royal Society of Chemistry (United Kingdom) under Grant Number R24-4761883271. Additional support was

received through the University of Pretoria Research Development Programme, which contributed significantly to the successful completion of this work.

References

1 J. Aravind kumar, T. Krithiga, S. Sathish, A. A. Renita, D. Prabu, S. Lokesh, R. Geetha, S. K. R. Namasivayam and M. Sillanpaa, *Sci. Total Environ.*, 2022, **831**, 154808.
2 A. Siddiqua, J. N. Hahladakis and W. A. K. A. Al-Attiya, *Environ. Sci. Pollut. Res.*, 2022, **29**, 58514–58536.
3 I. Staffell, D. Scamman, A. Velazquez Abad, P. Balcombe, P. E. Dodds, P. Ekins, N. Shah and K. R. Ward, *Energy Environ. Sci.*, 2019, **12**, 463–491.
4 Z. Yan, K. Yin, M. Xu, N. Fang, W. Yu, Y. Chu and S. Shu, *Chem. Eng. J.*, 2023, **472**, 145066.
5 B. Han, X. Shan, H. Xue, F. Liu, X. Song, J. Kong, Q. Lei, Y. Wang, D. Ma and Q. Zhang, *J. Environ. Sci.*, 2024, **153**, 202–216.
6 S. Balu, D. Ganapathy, S. Arya, R. Atchudan and A. K. Sundramoorthy, *RSC Adv.*, 2024, **14**, 14392–14424.
7 A. B, J. A, A. S. Rao, S. S. Nagarkar, A. Dutta, S. P. Duttagupta, S. S. Prabhu and R. Pinto, *Int. J. Hydrogen Energy*, 2024, **81**, 1442–1466.
8 S. B. Beil, S. Bonnet, C. Casadevall, R. J. Detz, F. Eisenreich, S. D. Glover, C. Kerzig, L. Næsborg, S. Pullen, G. Storch, N. Wei and C. Zeymer, *JACS Au*, 2024, **4**, 2746–2766.
9 D. Masekela, N. C. Hintsho-Mbita, S. Sam, T. L. Yusuf and N. Mabuba, *Arabian J. Chem.*, 2022, 104473.
10 L. Min, C. Hui, Z. Zhang and X. Wang, *Phys. Chem. Chem. Phys.*, 2023, **25**, 4388–4407.
11 Y. Yu, Z. Qiao and C. Ding, *Chem. Rec.*, 2024, **24**, e202400106.
12 T. Mohlala, T. L. Yusuf and N. Mabuba, *J. Electroanal. Chem.*, 2023, **947**, 117806.
13 T. L. Yusuf, B. Ojo, T. Mushiana, N. Mabuba, O. Arotiba and S. Makgato, *Catal. Sci. Technol.*, 2024, **14**, 6015–6026.
14 C. Nie, X. Wang, P. Lu, Y. Zhu, X. Li and H. Tang, *J. Mater. Sci. Technol.*, 2024, **169**, 182–192.
15 I. Ullah, M. Amin, P. Zhao, N. Qin and A.-W. Xu, *Inorg. Chem. Front.*, 2025, **12**, 1329–1348.
16 S. K. Sahoo, L. Acharya, L. Biswal, P. Priyadarshini and K. Parida, *Inorg. Chem. Front.*, 2024, **11**, 4914–4973.
17 T. L. Yusuf, O. C. Olalekan, D. Masekela, N. Mabuba, D. Onwudiwe and S. Makgato, *Ceram. Int.*, 2024, DOI: 10.1016/j.ceramint.2024.08.397.
18 Y. Guo, Y. Ao, P. Wang and C. Wang, *Appl. Catal., B*, 2019, **254**, 479–490.
19 L. Jing, Y. Xu, M. Xie, J. Liu, J. Deng, L. Huang, H. Xu and H. Li, *Chem. Eng. J.*, 2019, **360**, 1601–1612.
20 R. Lucena, J. C. Conesa, I. Aguilera, P. Palacios and P. Wahnón, *J. Mater. Chem. A*, 2014, **2**, 8236–8245.
21 W. Chen, Y.-X. Hua, Y. Wang, T. Huang, T.-Y. Liu and X.-H. Liu, *J. Catal.*, 2017, **349**, 8–18.
22 Y. Zhang, Q. Zhang, K. Xing, Y. Xiao, M. Zhao and Y. Cun, *Catal. Commun.*, 2024, **186**, 106815.
23 K. D. Jayeola, D. S. Sipuka, T. I. Sebokolodi, O. V. Nkwachukwu, C. Muzenda, B. A. Koiki, J. O. Babalola, M. Zhou and O. A. Arotiba, *Chem. Eng. J.*, 2024, **479**, 147482.
24 R. M. Mohamed, A. A. Ismail, M. W. Kadi, A. S. Alresheedi and I. A. Mkhalid, *ACS Omega*, 2020, **5**, 33269–33279.
25 G. Zuo, Y. Fu, H. Zhou, J. Du, X. Ding and H. Ye, *J. Mater. Sci.: Mater. Electron.*, 2025, **36**, 745.
26 Q. Liu, S. Dong, H. Jin, S. Ke, L. Luo and T. Huang, *J. Environ. Chem. Eng.*, 2023, **11**, 111568.
27 S. Talam, S. R. Karumuri and N. Gunnam, *Int. Scholarly Res. Not.*, 2012, **2012**, 372505.
28 J. Zhou, F. Zhao, Y. Wang, Y. Zhang and L. Yang, *J. Lumin.*, 2007, **122**, 195–197.
29 S. Zheng, P. Lu, A. M. Idris, B. Chen, X. Jiang, G. Jiang, J. Wang, S. Li and Z. Li, *J. Mater. Chem. A*, 2025, **13**(7), 5346–5356.
30 F. Xu, K. Meng, B. Cheng, J. Yu and W. Ho, *ChemCatChem*, 2019, **11**, 465–472.
31 L. Wang, G. Yang, S. Peng, J. Wang, D. Ji, W. Yan and S. Ramakrishna, *Int. J. Hydrogen Energy*, 2017, **42**, 25882–25890.
32 W. Chen, T. Huang, Y.-X. Hua, T.-Y. Liu, X.-H. Liu and S.-M. Chen, *J. Hazard. Mater.*, 2016, **320**, 529–538.
33 H.-Y. Liu, C.-G. Niu, H. Guo, C. Liang, D.-W. Huang, L. Zhang, Y.-Y. Yang and L. Li, *J. Colloid Interface Sci.*, 2020, **576**, 264–279.
34 M. Zhu, Q. Liu, W. Chen, Y. Yin, L. Ge, H. Li and K. Wang, *ACS Appl. Mater. Interfaces*, 2017, **9**, 38832–38841.
35 Z.-w. Zhang, R.-t. Guo, J.-y. Tang, Y.-f. Miao, J.-w. Gu and W.-g. Pan, *J. CO_2 Util.*, 2021, **45**, 101453.
36 K. Davis, R. Yarbrough, M. Froeschle, J. White and H. Rathnayake, *RSC Adv.*, 2019, **9**, 14638–14648.
37 Q. Zhu, B. Qiu, H. Duan, Y. Gong, Z. Qin, B. Shen, M. Xing and J. Zhang, *Appl. Catal., B*, 2019, **259**, 118078.
38 X. Yue, S. Yi, R. Wang, Z. Zhang and S. Qiu, *Nano Energy*, 2018, **47**, 463–473.
39 C. Shi, N. Tang, S. Pu, H. Xin, L. Wu and X. Hou, *Chem. Eng. J.*, 2025, **503**, 158621.
40 P. Semeraro, S. Bettini, S. Sawalha, S. Pal, A. Licciulli, F. Marzo, N. Lovergine, L. Valli and G. Giancane, *Nanomaterials*, 2020, **10**, 1458.
41 Q. Gao, L. Zhou, S. Xu, S. Dai, Q. Zhu and Y. Li, *Environ. Sci.: Nano*, 2023, **10**, 581–594.
42 C. Jin, W. Li, Y. Chen, R. Li, J. Huo, Q. He and Y. Wang, *Ind. Eng. Chem. Res.*, 2020, **59**, 2860–2873.
43 Y. Zhang, Y. Wang, Y. Liu, S. Zhang, Y. Zhao and J. Zhang, *J. Materiomics*, 2024, 100985.
44 M. Wei, C.-F. Li, X.-R. Deng and H. Deng, *Energy Procedia*, 2012, **16**, 76–80.
45 Y. Chen, Q. Wang, H. Huang, J. Kou, C. Lu and Z. Xu, *Int. J. Hydrogen Energy*, 2021, **46**, 32514–32522.
46 Q. Su, Y. Li, R. Hu, F. Song, S. Liu, C. Guo, S. Zhu, W. Liu and J. Pan, *Adv. Sustainable Syst.*, 2020, **4**, 2000130.
47 A. E. Hassan, M. H. Elsayed, M. S. A. Hussien, M. G. Mohamed, S.-W. Kuo, H.-H. Chou, I. S. Yahia, T. A. Mohamed and Z. Wen, *Int. J. Hydrogen Energy*, 2023, **48**, 9620–9635.
48 S. P. Vattikuti, P. A. K. Reddy, J. Shim and C. Byon, *J. Mater. Sci.: Mater. Electron.*, 2018, **29**, 18760–18770.